

Complex X-ray spectral variability in Mkn 421 observed with *XMM-Newton*

S. Sembay¹, R. Edelson^{1,2}, A. Markowitz², R. G. Griffiths¹, and M. J. L. Turner¹

sse@star.le.ac.uk

ABSTRACT

The bright blazar Mkn 421 has been observed four times for uninterrupted durations of $\sim 9 - 13$ hr during the performance verification and calibration phases of the *XMM-Newton* mission. The source was strongly variable in all epochs, with variability amplitudes that generally increased to higher energy bands. Although the detailed relationship between soft (0.1–0.75 keV) and hard (2–10 keV) band differed from one epoch to the next, in no case was there any evidence for a measurable interband lag, with robust upper limits of $|\tau| < 0.08$ hr in the best-correlated light curves. This is in conflict with previous claims of both hard and soft lags of ~ 1 hr in this and other blazars. However, previous observations suffered a repeated 1.6 hr feature induced by the low-Earth orbital period, a feature that is not present in the uninterrupted *XMM-Newton* data. The new upper limit on $|\tau|$ leads to a lower limit on the magnetic field strength and Doppler factor of $B\delta^{1/3} \gtrsim 4.7$ G, mildly out of line with the predictions from a variety of homogeneous synchrotron self-Compton emission models in the literature of $B\delta^{1/3} = 0.2 - 0.8$ G. Time-dependent spectral fitting was performed on all epochs, and no detectable spectral hysteresis was seen. We note however that the source exhibited significantly different spectral evolutionary behavior from one epoch to the next, with the strongest correlations in the first and last and an actual divergence between soft and hard X-ray bands in the third. This indicates that the range of spectral variability behavior in Mkn 421 is not fully described in these short snippets; significantly longer uninterrupted light curves are required, and can be obtained with *XMM-Newton*.

Subject headings: BL Lacertae objects: general — BL Lacertae objects: individual (Mkn 421) — galaxies: active — X-rays: galaxies

¹X-ray Astronomy Group; Leicester University; Leicester LE1 7RH; United Kingdom

²Astronomy Department; University of California; Los Angeles, CA 90095-1562; USA

1. Introduction

Mkn 421 has a long history of observations at X-ray and other wavelengths. It is nearby ($z = 0.031$) and is generally the brightest BL Lacertae object in the X-ray sky. BL Lac objects are a sub-class of blazars; sources whose broad-band continuum emission are dominated by relatively featureless nonthermal radiation and which show rapid spectral variability with the characteristic timescale of variations typically decreasing with increasing energy.

The spectral energy distribution (SEDs) of blazars have two distinct peaks in νF_ν space; one in the IR/optical or UV/X-ray regime and one at higher energies in the X-ray/Gamma-ray regime. The lower energy component is probably incoherent synchrotron radiation and the high energy component Compton up-scattering of lower energy photons. It seems likely that the synchrotron photons provide the seeds for the Compton emission (the synchrotron self-Compton process), but this has not been unambiguously demonstrated. BL Lacs are often classified as LBLs (low-energy peaked BL Lacs) if the synchrotron component peaks in the IR/optical regime or HBLs if it peaks in the UV/X-ray, although the classes may be the extrema of a single population (e.g. Fossati et al. 1998). Mkn 421 is an HBL.

The rapid flux variability in blazars would require the luminosity to be highly super-Eddington if the emission was isotropic and it is generally assumed that the emission region moves at relativistic speeds towards the observer; an interpretation supported by observations of superluminal motion of radio knots in the jet-like structure of some radio galaxies.

Although the relativistic jet model provides a plausible explanation for the continuum properties of blazars, detailed physical constraints on the structure of the jets remain an elusive goal; *snap-shot* multi-wavelength spectra can be reproduced by a variety of jet models with different underlying assumptions. Studying the variability behaviour of both the spectrum and flux is therefore the most profitable way to constrain the various jet models. The relationship of the variations within different energy bands can, in principle, help to constrain the geometry of the emission region on the macroscopic scale and constrain the physical radiation and loss processes on the microscopic scale. For instance, X-ray variations in the HBL, PKS 2155–304, have been seen to lead those in the optical/UV (e.g., Edelson et al. 1995; Urry et al. 1997), supporting the view that the X-rays arise from the synchrotron component and not from Compton scattering from these lower-energy bands.

The X-ray spectral slope is especially sensitive to electron cooling timescales within the various models and observations of interband lags within this regime have often been interpreted in this context. Chiappetti et al. (1999) found that soft X-ray (0.1–1.5 keV) variations in PKS 2155–304 led hard X-ray (3.5–10 keV) variations by ~ 0.3 –4 hr and sug-

gested it could occur through radiative cooling if the electron population has a sharp break or low-energy cut-off. Historically, however, the source has not exhibited a consistent behaviour in this respect. X-ray flares have also been observed with the hard band leading the soft (Sembay et al. 1993).

Mkn 421 has also been the subject of a number of monitoring campaigns and shows a similar variety of behaviour between observations. Takahashi et al. (1996) found that the hard X-ray band led the soft, whereas Fossati et al. (2000a) found the soft band led the hard. Takahashi et al. (2000) reported both types of behaviour seen within a single very long observation (~ 11 days) of the source by *BeppoSAX* and *ASCA*.

Interpretation of interband lags can, however, be complicated by the fact that these observations have been made with low-Earth orbit satellites, resulting in periodic interruptions in the light curves every ~ 1.6 hr due to Earth-occultation. Edelson et al. (2001; hereafter E01) analysed uninterrupted *XMM-Newton* data on PKS 2155–304 and found no significant interband lag down to a reliable limit of ~ 0.3 hr, attributing the previous claims of lags on short time scales to a spurious signal induced into the CCF at the orbital period of the satellites. Takahashi et al. (2000) also noted the possibility of such an effect in their paper on Mkn 421. One advantage *XMM-Newton* has over previous X-ray missions for monitoring purposes is that it has a highly eccentric orbit with a 48 hour period, thus allowing much longer continuous observation periods. Nominally the only data gaps occur during passage through the radiation belts at perigee which takes around 7–8 hrs and, in the first year or so of the mission, a ~ 1 hour gap at apogee due to incomplete ground station coverage (Jansen et al. 2001).

XMM-Newton has observed both PKS 2155–304 and Mkn 421 on several occasions since launch. We have reported on the *XMM-Newton* observation of PKS 2155–304 in E01. In this paper we now present the results of several observations of Mkn 421. The observations and data reduction are discussed in the next section. The temporal analysis of these data are reported and compared with other data in § 3. The spectral analysis is discussed in § 4 and a concluding discussion is given in § 5.

2. Observations and Data Analysis

2.1. Observations

The *XMM-Newton* observations of Mkn 421 were performed as part of the performance-verification and calibration programme. The source was observed on-axis on four occasions at the epochs listed in Table 1. *XMM-Newton* has three co-aligned X-ray telescopes with

focal plane cameras of two types; two EPIC–MOS imaging CCD cameras and one EPIC–pn imaging CCD camera (Turner et al. 2001; Strüder et al. 2001). Within the telescopes containing the MOS cameras, gratings divert approximately half the incident flux to two Reflection Grating Spectrometer (RGS) instruments (den Herder et al. 2001).

In this paper our analysis concentrates on data taken with the high–throughput EPIC CCD cameras. The EPIC cameras have superior sensitivity to short timescale flux variations and a broader energy response than the RGS instruments. During orbital revolutions 165, 171 and 259 (henceforth, O165, O171 and O259) both EPIC cameras were in their respective Small Window (SW) imaging modes throughout the observation. In orbit 84 (O84), however, the first part of the observation was performed in timing mode for the pn and MOS1 cameras, and SW mode for MOS2, followed by SW mode for the pn and MOS1 and timing mode for MOS2. There is, however, only a small overlap of about 5 ksec between the pn and MOS imaging data. Due to a radiation alert the MOS cameras were switched off shortly after the beginning of the pn SW mode observation (further details of the O84 observation can be found in Brinkmann et al. (2001) which gives the first analysis of the data from this observation). A variety of blocking filters were employed throughout the observations and these are listed in Table 1.

The data analysis software and calibration were generally in a more mature state for imaging mode than timing mode when the analysis was performed, so this paper deals with the imaging data only.

The imaging observations were performed in each instrument’s SW mode because they have a faster CCD frame readout time than their respective Full–Frame modes. This mode reduces the effects of pulse pile–up which causes spectral distortion in bright sources. Pulse pile–up occurs when two (or more) X–rays interact within a given frame close enough such that their deposited charge distributions overlap. This can lead to a loss of flux if the resultant charge distribution does not have a valid pattern within the instruments X–ray pattern library, or, if it still has a valid pattern, a new event whose energy is the sum of the contributing events. Hence, pile–up leads to an artificial hardening of the spectrum and can produce spurious correlations between soft and hard–band variations. The simplest way to correct for pile–up is to exclude the core of the point–spread function where pile–up is greatest. This is explained in more detail in the following Section.

The pn SW mode has a 63×64 pixel window (equivalent to $\sim 4.3 \times 4.4$ arcminutes on the sky) with a frame readout time of 5.7 ms. The common telescope boresight places the source off–centre within the window, typically less than an arcminute from the CCD boundary. For the MOS cameras the window is 100×100 pixels ($\sim 1.8 \times 1.8$ arcminutes), more centered with respect to the boresight, and the mode has a frame readout time of 0.3 s.

2.2. Data Reduction

A standard reduction of the raw pn and MOS event lists was performed using the Science Analysis System (SAS) Version 5.2. The SAS removes events from the location of defective pixels, corrects for charge transfer losses across the CCDs and applies a gain calibration to convert the recorded charge in ADC units to a pulse-invariant energy scale. Standard analysis packages are then used to create images, light-curves and spectra from the calibrated event lists.

Pulse pile-up in CCD detectors is nominally a purely statistical effect which can in principle be corrected for by modifying the instrument response function appropriately. However, without having a suitable tool available within the SAS, we have used the more direct approach of excluding events from the core of the point-spread function where, naturally, pile-up is the most extreme. Although this leads to a loss of flux, the high throughput of XMM means that we are still left with spectra and light curves with high statistical significance.

The size of the core to be excluded was determined by examining the distribution of mono-pixel to multi-pixel events as a function of energy. As the radius of the excluded region is increased, the distribution tends towards that consistent with the theoretical distribution for the non piled-up case. By this method we excluded core radii of diameter 8", 6", 10" and 10" respectively for the pn O84, O165, O171 and O259 observations and 8", 12" and 12" for the MOS O165, O171 and O259 observations. The maximum radius of each annulus was 36.75" during O84 increasing to 44" for the remaining observations; the difference being due to a change in the relative boresight with respect to the pn window.

The point-spread function of each telescope is energy dependant so a correction needs to be applied to the effective area of the response file when fitting spectra extracted from an annulus with a given inner and outer radius. To do this we used a description of the psf developed by the EPIC instrument teams using in-flight data from several on-axis point sources (Ghizzardi & Molendi 2002). The robustness of this procedure and other calibration related issues are discussed in more detail in Section 4.

In table 1 we list the mean observed 0.1 – 10.0 keV source count rates (obtained *after* excluding the psf cores) during each observation. The source was most luminous during O171, but only $\sim 1/3$ as bright twelve days earlier during O165. O84 and O259 are at intermediate levels. The higher observed count rate in the soft band during O259 is primarily a consequence of the higher throughput of the Thin blocking filter compared with the Medium and Thick filters used earlier.

3. Timing Analysis

In this section, we compare gross variability in different energy bands for each of the observing epochs. Much of this analysis parallels that on PKS 2155–304 by E01. Although most of the analyses will be restricted to higher signal-to-noise pn data, the relevant MOS data are also included for consistency.

The light curves were constructed as follows: first, data were divided into soft (S; 0.1–0.75 keV), medium (M; 0.9–1.7 keV) and hard (H; 2–10 keV) bands. Then, the data were initially extracted at 1 sec intervals. They were then rebinned to 300 sec resolution and standard methods were used to measure the mean and standard errors from the spread of data in each bin. Due to data loss, there were two small gaps in the O165 light curves. The four points during 1.75–2.00 hrs and three points during 5.08–5.25 hrs after the beginning of the integration were instead determined by interpolation from the surrounding points.

In all bands, the source count rate exceeded the background by at least a factor of $\sim 50 - 100$, so no background light curves were extracted. The resulting light curves are shown in Figure 1.

3.1. Variability Amplitudes

Variability amplitudes were measured for each light curve using the fractional variability amplitude, defined as

$$f_v = \frac{\sqrt{S^2 - \langle \sigma_{err}^2 \rangle}}{\langle X \rangle}, \quad (1)$$

where S^2 is the total measured variance, $\langle \sigma_{err}^2 \rangle$ is the mean squared errors, and $\langle X \rangle$ is the mean count rate (see E01 for details). The fractional variability amplitude is also simply the square-root of the “excess variance” parameter used e.g., in Nandra et al. (1999); $f_v = \sqrt{\sigma_{xs}^2}$. These quantities are computed and shown in Table 2. Examination of this and Figure 1 indicate that stronger variations are clearly seen in the harder bands. This increasing variability with energy band is common in blazars (e.g., Ulrich, Maraschi & Urry 1997) and is a consequence of the fact that high energy electrons have shorter cooling timescales than low energy ones. Finally, different variability levels are seen in each of the epochs with O84 exhibiting the greatest overall degree of flux variations.

3.2. Comparison of the Hard and Soft Light Curves

Figure 2 shows a variety of quantities derived directly from the light curves in Figure 1. The top panel gives the geometric mean flux of the three bands, $F_g = \sqrt[3]{F_H \times F_M \times F_S}$. The second panel is the hardness ratio, $HR = F_H/F_S$. Note that the mean and hardness ratio light curves generally track each other very well, confirming that the source generally gets harder as it gets brighter, with the exception of the end of O165 where we observe a softening of the source as it continues to brighten.

Below that is an “overplot” diagram for the hard and soft bands. In these the light curves are subjected to the first two steps of cross-correlation function (CCF) analysis: at each point in the light curve, the mean count rate is subtracted and then the data are divided by the standard deviation. The resulting plot, with zero mean and unit variance for each light curve, provides a both a simple way to compare variations between bands as well as a convenient “sanity check” of the final CCFs by showing the intermediate step. Finally, the bottom panel is the difference between the two scaled light curves.

The temporal relation between hard and soft band variations shows a range of behaviors: O84: almost perfect agreement to within the errors; O165 and 259: good general agreement but significant divergences on short (\gtrsim hour) time scales; O171: poor overall agreement and even a divergence between soft and hard bands. As seen below, the light curves that track the best (O84 and O259) are particularly useful because they allow the finest measurement/limits on the interband lag.

3.3. Cross-Correlation Analysis

Cross-correlation functions were measured using the discrete correlation function (DCF; Edelson & Krolik 1989) and the interpolated correlation function (ICF; White & Peterson 1994). These are shown in Figure 3, where a positive τ indicates that the softer band leads the harder band. They are also tabulated in Table 3. The errors, measured using the bootstrap method of Peterson et al. (1998), indicate a 2σ upper limit of $\tau \leq 0.08$ hr.

The best-tracking epoch (O84) also showed the highest correlation coefficients ($r \geq 0.99$) and the strongest limits on the interband lags ($\bar{\tau} = -0.01 \pm 0.03$). Such similar limits are seen in the next two strongest correlations (O165 S/M and O259 M/H, with $r = 0.96$) and for the eight highest correlations (out of 12, those with $r \geq 0.89$, $\bar{\tau} = -0.01 \pm 0.04$). Recall that the bin size is 0.08 hr (300 sec); these indicate very secure ($2 - 3\sigma$) limits of $|\tau| < 0.08$ hr).

However, it is also clear especially in O171 that the hard and soft light curves are not

always tracking each other with high precision. In this case, the hard and soft actually diverge, and the peak correlation function is less than zero. This reveals a further complexity in the spectral variability that cannot be addressed with these short snippets of data, and indicates the need for much longer uninterrupted observations to fully describe the observational picture.

3.4. Comparison with Previous Results

Previous observations of Mkn 421 have claimed significant hard lags, in which the hard band lagged behind the soft by ~ 0.6 hr (Fossati et al. 2000a), as well as soft lags, in which the soft band lagged behind the hard by ~ 1 hr. By comparison, this paper finds that only during one of the four epochs are the data sufficiently well correlated to measure a meaningful CCF, and in that case, there is no measurable interband lag down to much tighter 2σ limits: $|\tau| \leq 0.08$ hr (1 bin width).

In order to understand this discrepancy, it is important to keep in mind that the previous claims of interband lags all involved observations made with low-Earth orbit satellites (*Bep-poSAX* and *ASCA*). As pointed out by E01, CCFs measured from such data are corrupted on time scales less than the orbital period (1.6 hr) and thus can yield spurious apparent lags. This can be seen in Figure 11 of Fossati et al. (2000a): there is a periodic feature running through the CCF with a period of 1.6 hr, causing excursions larger than any claimed local peaks. Indeed, the highest point in that CCF is at zero lag, and the next two highest points are immediately beside it. On the other hand, *XMM-Newton* produces uninterrupted light curves that do not suffer from this systematic errors, so the CCFs are intrinsically more reliable. Thus, we conclude that there is no reliable evidence for interband lags, hard or soft, in Mkn 421.

4. Spectral Analysis

The intrinsic X-ray spectra of BL Lacs are basically smooth and featureless. Over an energy band of roughly a decade the continuum can be well represented by a power law model whereas over a wider band the continuum exhibits a degree of curvature requiring fitting by broken-power law or continuously curved (CC) spectral models (e.g. Inoue & Takahara 1996; Fossati et al. 2000b). In this paper we have confined our analysis to the high energy 2.0 to 10 keV spectral band. There are unresolved cross-calibration issues between the EPIC instruments in the soft band which lead to somewhat contradictory results regarding the

slope of the low-energy continuum. A full analysis of the entire spectral range will be left to a later paper. In the chosen band, the derived spectra can be fit a single power law with the column density fixed at the Galactic line-of-sight value of $1.6 \times 10^{20} \text{ cm}^2$ (Lockman & Savage 1995) which is in agreement with previous spectral analyses of the broad-band X-ray spectrum (e.g. Fossati et al. 2000b).

Our spectral analysis on Mrk 421 proceeded as follows. Having removed the piled-up section of the point spread function as described earlier, we subdivided each observation into 5 ksec segments. This allowed us to extract spectra with good statistical significance and still track spectral variations throughout each observation. Between six and nine spectra were extracted per observation and per camera. For completeness, background spectra were extracted, but the background rate was found to be negligible with respect to the source and hence the background spectra were ignored. The pn data were analysed separately to the MOS, but the data from both MOS cameras were combined in the spectral fitting. All spectral fitting was done with Xspec Version 11.00.

Table 4 lists the derived spectral parameters from each fit. There is an excellent agreement between the pn and MOS parameters in general. The pn photon indices for example are typically within $\Delta\alpha \sim 0.05$ of the MOS. The overall range in 2-10 keV source flux is similar to that observed in the *BeppoSAX* campaigns of 1997 and 1998 (Fossati et al. 2000b).

In Figure 4 we have plotted the spectral index from all observations, against the 2 to 10 keV (deabsorbed) flux. For clarity, the epic-pn parameters only are plotted. From this plot we can see that although the variation of slope with flux follows in general the classical trend of synchrotron emission, namely, that steeper slopes correspond with lower flux states, there is no strong correlation between these parameters globally. As expected from the previous discussion of the light curves, the variability behaviour is quite different between observations. In O84 the slope is stable but the flux varies. In O165, when the source was weakest and the spectrum steepest, neither parameter varied strongly. O171 and O259 show a similar behaviour in that a fairly linear correlation between slope and flux is evident.

5. Discussion

The temporal analysis found that in O84, the data were highly correlated with no evidence for an interband lag down to time scales of $|\tau| \leq 0.08 \text{ hr}$, much tighter limits than previous claims of both hard and soft lags. Following on from similar results on PKS 2155–304 by E01 this provides further strong evidence that the detection of lags on short time scales by low-Earth orbit satellites are probably spurious artefacts caused by Earth occultation.

Measurements of a lag could potentially give the cooling time scale and therefore a limit on the magnetic field strength assuming that the lag is due to the electron population softening due to radiative losses. From Chiappetti et al. (1999),

$$B\delta^{1/3} = 300 \left(\frac{1+z}{\nu_1} \right)^{1/3} \left(\frac{1 - (\nu_1/\nu_0)^{1/2}}{\tau} \right)^{2/3} G, \quad (2)$$

where B is the magnetic field strength, δ is the Doppler factor, z is the redshift, and ν_1 and ν_0 are the frequencies (in units of 10^{17} Hz) at which a lag, τ , is measured. For the Orbit 84 measurement, we have an upper limit on the lag so we can derive a lower limit on the value of $B\delta^{1/3}$. The most stringent limit is given by the hard and soft light curves with $\nu_0 \sim 14.5$ and $\nu_1 \sim 1.0$, $z = 0.031$ and $\tau \lesssim 300$ s giving $B\delta^{1/3} \gtrsim 4.7$ G.

This lower limit is rather higher (typically by a factor of $\sim 5 - 10$) than obtained from some estimates of B and δ in the literature derived from fitting a variety of homogeneous SSC models to measurements of the broad-band SED of Mkn 421 observed at different epochs. For example, Ghisellini et al. (1998) obtain $B = 0.09$ G and $\delta = 12$ giving $B\delta^{1/3} = 0.2$ G for a pure SSC model. If the seed photons of the Compton emission arise from an external source (e.g. an accretion disk or the broad-line region) then the model allows for a somewhat higher magnetic field strength. In this case Ghisellini et al. (1998) obtain $B = 0.22$ G and $\delta = 11$ giving $B\delta^{1/3} = 0.49$ G. In comparison, Tavecchio, Maraschi and Ghisellini (1998), obtained $B = 0.25$ G and $\delta = 25$ giving $B\delta^{1/3} = 0.7$ G, also with a homogeneous SSC model, and Krawczynski et al. (2002) argue for $B = 0.22$ G and $\delta \sim 50$ which gives $B\delta^{1/3} = 0.8$ G.

Despite the differences in the underlying assumptions behind the specific homogeneous models employed a rather narrow range of values of $B\delta^{1/3}$ are predicted. It is possible that source variability is the cause of the discrepancy with, perhaps, the magnetic field strength during O84 being unusually high compared with earlier epochs. Unfortunately we have no way to directly test this because we have no simultaneous observations in the gamma-ray regime with the O84 observation. The Krawczynski et al. (2002) paper does deal with simultaneous X-ray and TeV gamma-ray observations (obtained with *RXTE*, the *Rossi X-ray Timing Explorer* and HEGRA, the High Energy Gamma Ray Astronomy experiment) taken in February and 3-8th May 2000, which is close to, but not contemporaneous with the 25th May 2000 O84 observation. Appealing to source variability, however, seems contrived given the fact that observations from different epochs are returning a similar range of magnetic field strengths. The previous claims of lags on longer, ~ 1 hr, timescales lead to values of the B and δ combination that are consistent with these models and this has been used as an argument in their favour on the grounds of self-consistency. Our much tighter upper limit on the lag may, however, indicate a possible incompatibility with the homogeneous SSC model

although the results are not conclusive.

It is interesting that even in these short *XMM-Newton* observations the spectral variability behaviour of Mkn 421 is quite complex. Of special interest is the lack of any obvious spectral hysteresis in the variation of intensity with slope as has been commonly observed in a number of blazars, including Mkn 421 (e.g. Sembay et al. 1993, Takahashi et al. 1996). When observed it most commonly follows a clockwise loop in the sense of Figure 4. This behaviour naturally follows whenever the slope is controlled by cooling processes which act faster at higher energies, as is the case when synchrotron cooling dominates. If the system is in a regime where the cooling and acceleration times are equal, however, the reverse behaviour is expected and the slope will track the intensity in an anticlockwise loop (Kirk, Rieger & Mastichiadis 1998).

There are a number of possible reasons why our observations show no clean examples of hysteresis. First, it may simply be that the observations are too short relative to the characteristic flaring timescale and therefore we are observing only partial segments of a given loop. This may explain the difference in the 2-10 keV spectral behaviour between O84 and O171 which both show a decay in flux. In the latter case the observation may be starting from near the peak intensity where a rapid change in slope would be expected during the initial decay. In the former we may be well below the peak intensity in a segment where we expect only a minor change in slope (see Figure 3 from Kirk, Rieger & Mastichiadis 1998). Second, there may be contributions from multiple flares at different phases of their cycle; the lack of a correlation between the soft and hard bands in O171 appears to show an independent soft flaring component. Finally, the system overall may physically be in a transition zone between characteristically clockwise and anticlockwise spectral behaviour.

Attempts have been made to monitor Mkn 421 and other BL Lacs with long observations by *BeppoSAX* and *ASCA* however, these are limited on what they could achieve on analysing short time scales by being interrupted by Earth occultation. *XMM-Newton* can provide the uninterrupted light curves on the short time scales required to unambiguously test for the presence of X-ray lags, but a source such as Mkn 421 needs to be monitored for longer than the observations presented in this paper (which were designed primarily for instrument calibration purposes) in order to track the source behaviour over a wider range of time scales.

The authors thank the *XMM-Newton* team for the huge amount of effort required to build and operate this complex and powerful instrument. Sembay, Griffiths and Turner acknowledge financial support from the UK Particle Physics and Astronomy Research Council. Edelson and Markowitz are supported by NASA grants NAG 5-7317 and NAG 5-9023.

REFERENCES

- Brinkmann, W., Sembay, S., Griffiths, R. G., Branduardi-Raymont, G., Gliozzi, M., Boller, Th., Tiengo, A., Molendi, S., & Zane, S. 2001, *A&A*, 365, L162
- Chiappetti, L. et al. 1999, *ApJ*, 521, 552
- de Herder, J.W. et al. 2001, *A&A*, 365, L7
- Edelson, R., & Krolik, J. 1989, *ApJ*, 333, 646
- Edelson, R. et al. 1995, *ApJ*, 438, 120
- Edelson, R., Griffiths, G., Markowitz, A., Sembay, S., Turner, M. J. L., & Warwick, R. 2001, *ApJ*, 554, 274 (E01)
- Fossati, G. et al. 1998, *MNRAS*, 299, 433
- Fossati, G., Celotti, A., Chiaberge, M., Zhang, Y. H., Chiappetti, L., Ghisellini, G., Maraschi, L., Tavecchio, F., Pian, E., & Treves, A. 2000a, *ApJ*, 541, 153
- Fossati, G., Celotti, A., Chiaberge, M., Zhang, Y. H., Chiappetti, L., Ghisellini, G., Maraschi, L., Tavecchio, F., Pian, E., & Treves, A. 2000b, *ApJ*, 541, 166
- Ghisellini, G., Celotti, A., Fossati, G., Maraschi, L., & Comastri, A. 1998, *MNRAS*, 451, 468
- Ghizzardi, S. & Molendi, S. 2002, *New Visions of the X-ray Universe in the XMM-Newton and Chandra era*, 26-30 November 2001, ESTEC, The Netherlands. *in press*
- Inoue, S. & Takahara, F. 1996, *ApJ*, 463, 555
- Jansen, F. et al. 2001, *A&A*, 365, L1
- Kataoka, J. et al. 2000, *ApJ*, 528, 243
- Kirk, J. G., Rieger, F. M., & Mastichiadis, A. 1998, *A&A*, 333, 452
- Krawczynski, H. et al. 2002, *ApJ*, *in press*
- Lockman, F. J. & Savage, B. D. 1995, *ApJS*, 97, 1
- Peterson, B. M. et al. 1998, *PASP*, 110, 660
- Sembay, S., Warwick, R. S., Urry, C. M., Sokoloski, J., George, I. M., Makino, F., Ohashi, T., & Tashiro, M. 1993, *ApJ*, 404, 112
- Strüder, L. et al. 2001, *A&A*, 365 L18
- Takahashi, T., Tashiro, M., Madejski, G., Kubo, H., Kamae, T., Kataoka, J., Kii, T., Makino, F., Makishima, K., & Yamasaki, N. 1996, *ApJ*, 470, 89
- Takahashi, T. et al. 2000, *ApJ*, 542, 105

- Tavecchio, F., Maraschi, L., & Ghisellini, G. 1998, ApJ, 509, 608
Turner, M. J. L. et al. 2001, A&A, 365, L27
Ulrich, M.-H., Maraschi, L., & Urry, C. M. 1997, ARA&A, 35, 445
Urry, C. M. et al. 1997, ApJ, 486, 799
White, R., & Peterson, B. M. 1994, PASP, 106, 879

Table 1. Observation Summary

Orbit	Inst.	Observing Time 2000 UT	Mode	Filter	0.1–10 keV $\langle \text{cts s}^{-1} \rangle$
84	pn	05 25 10:35:19 – 05 25 19:36:58	SW	Medium	88.65
165	pn	11 01 23:48:12 – 11 02 10:04:14	SW	Thick	51.07
171	pn	11 13 22:00:50 – 11 13 10:57:29	SW	Thick	125.23
259	pn	05 08 09:31:39 – 05 08 19:58:33	SW	Thin	130.82
165	MOS1	11 01 23:47:12 – 11 02 10:09:02	SW	Medium	18.87
165	MOS2	11 01 23:47:12 – 11 02 10:09:00	SW	Medium	18.62
171	MOS1	11 13 22:00:52 – 11 14 11:11:37	SW	Medium	38.52
171	MOS2	11-13 22:00:53 – 11 14 11:11:38	SW	Medium	37.93
259	MOS1	05 08 09:16:05 – 05 08 19:56:13	SW	Thin	31.25
259	MOS2	05 08 09:16:04 – 05 08 19:56:13	SW	Thin	31.64

Table 2. Variability Parameters

Orbit	Band	Npts	$\langle X \rangle$ cts s ⁻¹	σ_{xs}^2 $\times 10^{-3}$	F _{var} ¹	S/N
84	pn-S	109	41.82	4.95 ± 0.34	7.03 ± 0.49 %	106.10
84	pn-M	109	24.44	12.78 ± 0.88	11.31 ± 0.78 %	81.41
84	pn-H	109	10.62	23.71 ± 1.63	15.40 ± 1.06 %	53.59
165	pn-S	123	26.97	5.96 ± 0.39	7.72 ± 0.52 %	87.20
165	pn-M	123	13.11	7.16 ± 0.47	8.46 ± 0.56 %	60.44
165	pn-H	123	4.55	7.71 ± 0.54	8.78 ± 0.62 %	36.01
171	pn-S	156	58.08	0.62 ± 0.04	2.49 ± 0.16 %	114.13
171	pn-M	156	35.21	1.52 ± 0.09	3.90 ± 0.24 %	88.59
171	pn-H	156	14.92	14.23 ± 0.82	11.93 ± 0.69 %	58.82
259	pn-S	126	75.74	1.31 ± 0.09	3.62 ± 0.24 %	147.81
259	pn-M	126	28.83	4.22 ± 0.27	6.50 ± 0.42 %	90.91
259	pn-H	126	11.60	14.44 ± 0.93	12.02 ± 0.77 %	58.36
165	MOS-S	125	18.23	5.37 ± 0.36	7.33 ± 0.49 %	64.62
165	MOS-M	125	10.89	7.44 ± 0.49	8.62 ± 0.57 %	53.22
165	MOS-H	125	4.47	4.22 ± 0.31	6.50 ± 0.48 %	39.22
171	MOS-S	157	31.23	1.02 ± 0.07	3.20 ± 0.21 %	84.39
171	MOS-M	157	24.51	1.10 ± 0.07	3.32 ± 0.22 %	77.74
171	MOS-H	157	10.43	10.08 ± 0.59	10.04 ± 0.59 %	54.50
259	MOS-S	128	28.85	1.17 ± 0.08	3.42 ± 0.24 %	78.01
259	MOS-M	128	18.57	4.30 ± 0.28	6.55 ± 0.43 %	68.95
259	MOS-H	128	7.69	15.73 ± 1.01	12.54 ± 0.81 %	45.61

Table 3. Cross-Correlation Results

Rev.	Instr.	Band 1 (keV)	Band 2 (keV)	DCF r_{max}	DCF τ (hr)	ICF r_{max}	ICF τ (hr)
84	pn	0.1-0.75	0.9-1.7	0.99	0.00	0.99	+0.04 \pm 0.05
84	pn	0.1-0.75	2-10	0.98	-0.08	0.99	-0.04 \pm 0.04
84	pn	0.9-1.7	2-10	0.98	-0.08	0.99	-0.04 \pm 0.04
165	pn	0.1-0.75	0.9-1.7	0.96	-0.08	0.96	-0.04 \pm 0.08
165	pn	0.1-0.75	2-10	0.83	-0.75	0.83	-0.71 \pm 0.52
165	pn	0.9-1.7	2-10	0.88	-0.17	0.89	-0.21 \pm 0.18
171	pn	0.1-0.75	0.9-1.7	0.24	-6.00	0.29	+6.42 \pm 5.75
171	pn	0.1-0.75	2-10	0.12	+6.33	0.17	+6.42 \pm 5.65
171	pn	0.9-1.7	2-10	0.87	0.00	0.89	+0.04 \pm 0.08
259	pn	0.1-0.75	0.9-1.7	0.90	+0.08	0.91	+0.13 \pm 0.06
259	pn	0.1-0.75	2-10	0.84	+0.17	0.85	+0.13 \pm 0.07
259	pn	0.9-1.7	2-10	0.96	0.00	0.96	+0.04 \pm 0.04

Note. — A positive lag indicates the softer band leading the harder band (hard band is delayed with respect to soft band). DCF bin size is the resolution of the lightcurve, 300 sec.; ICF resolution is one half the DCF bin size.

Table 4. Spectral Fits

Bin	EPIC-pn				EPIC-MOS			
	Γ	Norm (1 keV)	Flux ^b 2.0-10.0	χ^2_{ν}	Γ	Norm (1 keV)	Flux ^b 2.0-10.0	χ^2_{ν}
Orbit 84								
1	$2.24^{+0.02}_{-0.02}$	$0.185^{+0.004}_{-0.004}$	3.34	1.05	-	-	-	-
2	$2.22^{+0.02}_{-0.02}$	$0.156^{+0.004}_{-0.004}$	2.92	0.97	-	-	-	-
3	$2.22^{+0.02}_{-0.02}$	$0.132^{+0.003}_{-0.003}$	2.45	1.04	-	-	-	-
4	$2.20^{+0.02}_{-0.02}$	$0.120^{+0.003}_{-0.003}$	2.29	1.16	-	-	-	-
5	$2.20^{+0.02}_{-0.02}$	$0.124^{+0.003}_{-0.003}$	2.39	1.02	-	-	-	-
6	$2.27^{+0.02}_{-0.02}$	$0.134^{+0.003}_{-0.003}$	2.34	1.02	-	-	-	-
Orbit 165								
1	$2.55^{+0.03}_{-0.03}$	$0.063^{+0.002}_{-0.002}$	0.73	0.99	$2.53^{+0.04}_{-0.04}$	$0.061^{+0.003}_{-0.003}$	0.73	0.96
2	$2.55^{+0.03}_{-0.03}$	$0.057^{+0.002}_{-0.002}$	0.66	1.01	$2.51^{+0.05}_{-0.05}$	$0.055^{+0.003}_{-0.003}$	0.67	1.09
3	$2.50^{+0.03}_{-0.03}$	$0.055^{+0.002}_{-0.002}$	0.69	1.10	$2.46^{+0.04}_{-0.04}$	$0.053^{+0.002}_{-0.002}$	0.71	1.08
4	$2.52^{+0.03}_{-0.03}$	$0.060^{+0.002}_{-0.002}$	0.74	1.02	$2.47^{+0.04}_{-0.04}$	$0.058^{+0.003}_{-0.003}$	0.77	0.98
5	$2.50^{+0.03}_{-0.03}$	$0.067^{+0.002}_{-0.002}$	0.83	0.94	$2.42^{+0.03}_{-0.03}$	$0.062^{+0.002}_{-0.002}$	0.87	0.87
6	$2.47^{+0.03}_{-0.03}$	$0.067^{+0.002}_{-0.002}$	0.87	1.05	$2.46^{+0.03}_{-0.03}$	$0.066^{+0.003}_{-0.003}$	0.87	0.98
7	$2.51^{+0.03}_{-0.03}$	$0.066^{+0.002}_{-0.002}$	0.81	1.03	$2.53^{+0.03}_{-0.04}$	$0.070^{+0.003}_{-0.003}$	0.83	1.09
Orbit 171								
1	$2.20^{+0.02}_{-0.02}$	$0.222^{+0.005}_{-0.005}$	4.23	1.16	$2.19^{+0.02}_{-0.02}$	$0.213^{+0.005}_{-0.005}$	4.14	1.02
2	$2.20^{+0.02}_{-0.02}$	$0.218^{+0.004}_{-0.005}$	4.18	1.03	$2.20^{+0.02}_{-0.02}$	$0.216^{+0.005}_{-0.005}$	4.16	1.16
3	$2.23^{+0.02}_{-0.02}$	$0.211^{+0.004}_{-0.005}$	3.89	1.07	$2.22^{+0.02}_{-0.02}$	$0.206^{+0.005}_{-0.005}$	3.82	1.23
4	$2.37^{+0.02}_{-0.02}$	$0.229^{+0.005}_{-0.005}$	3.47	1.05	$2.33^{+0.02}_{-0.02}$	$0.221^{+0.005}_{-0.005}$	3.51	1.21
5	$2.39^{+0.02}_{-0.02}$	$0.224^{+0.005}_{-0.005}$	3.30	1.06	$2.36^{+0.02}_{-0.02}$	$0.220^{+0.005}_{-0.005}$	3.37	0.94
6	$2.39^{+0.02}_{-0.02}$	$0.224^{+0.005}_{-0.005}$	3.29	1.00	$2.38^{+0.02}_{-0.02}$	$0.225^{+0.005}_{-0.006}$	3.35	0.90
7	$2.42^{+0.02}_{-0.02}$	$0.223^{+0.005}_{-0.005}$	3.13	0.97	$2.40^{+0.02}_{-0.02}$	$0.219^{+0.005}_{-0.006}$	3.17	1.01
8	$2.47^{+0.02}_{-0.02}$	$0.213^{+0.005}_{-0.005}$	2.78	1.09	$2.45^{+0.02}_{-0.02}$	$0.212^{+0.006}_{-0.006}$	2.83	1.15
9	$2.49^{+0.02}_{-0.02}$	$0.223^{+0.005}_{-0.005}$	2.85	1.11	$2.44^{+0.02}_{-0.02}$	$0.221^{+0.006}_{-0.006}$	3.01	1.12
Orbit 259								
1	$2.37^{+0.02}_{-0.02}$	$0.145^{+0.003}_{-0.004}$	2.16	1.05	$2.38^{+0.03}_{-0.03}$	$0.148^{+0.004}_{-0.004}$	2.20	0.95
2	$2.25^{+0.02}_{-0.02}$	$0.147^{+0.003}_{-0.003}$	2.64	1.11	$2.26^{+0.03}_{-0.02}$	$0.156^{+0.004}_{-0.004}$	2.74	1.10
3	$2.21^{+0.02}_{-0.02}$	$0.148^{+0.003}_{-0.003}$	2.79	1.02	$2.24^{+0.02}_{-0.02}$	$0.155^{+0.004}_{-0.004}$	2.81	1.09
4	$2.20^{+0.02}_{-0.02}$	$0.141^{+0.003}_{-0.003}$	2.70	1.03	$2.24^{+0.02}_{-0.02}$	$0.150^{+0.004}_{-0.004}$	2.73	1.05
5	$2.20^{+0.02}_{-0.02}$	$0.148^{+0.003}_{-0.003}$	2.87	0.93	$2.19^{+0.02}_{-0.02}$	$0.154^{+0.004}_{-0.004}$	2.97	1.16
6	$2.23^{+0.02}_{-0.02}$	$0.157^{+0.003}_{-0.003}$	2.86	1.00	$2.24^{+0.02}_{-0.02}$	$0.160^{+0.004}_{-0.004}$	2.90	1.00
7	$2.34^{+0.02}_{-0.02}$	$0.145^{+0.004}_{-0.004}$	2.27	1.13	$2.38^{+0.03}_{-0.03}$	$0.156^{+0.004}_{-0.005}$	2.31	1.02

Note. — a) All errors are 1σ for two interesting parameters ($\delta\chi^2 = 2.30$). b) Deabsorbed flux in units of 10^{-10} erg cm⁻² s⁻¹

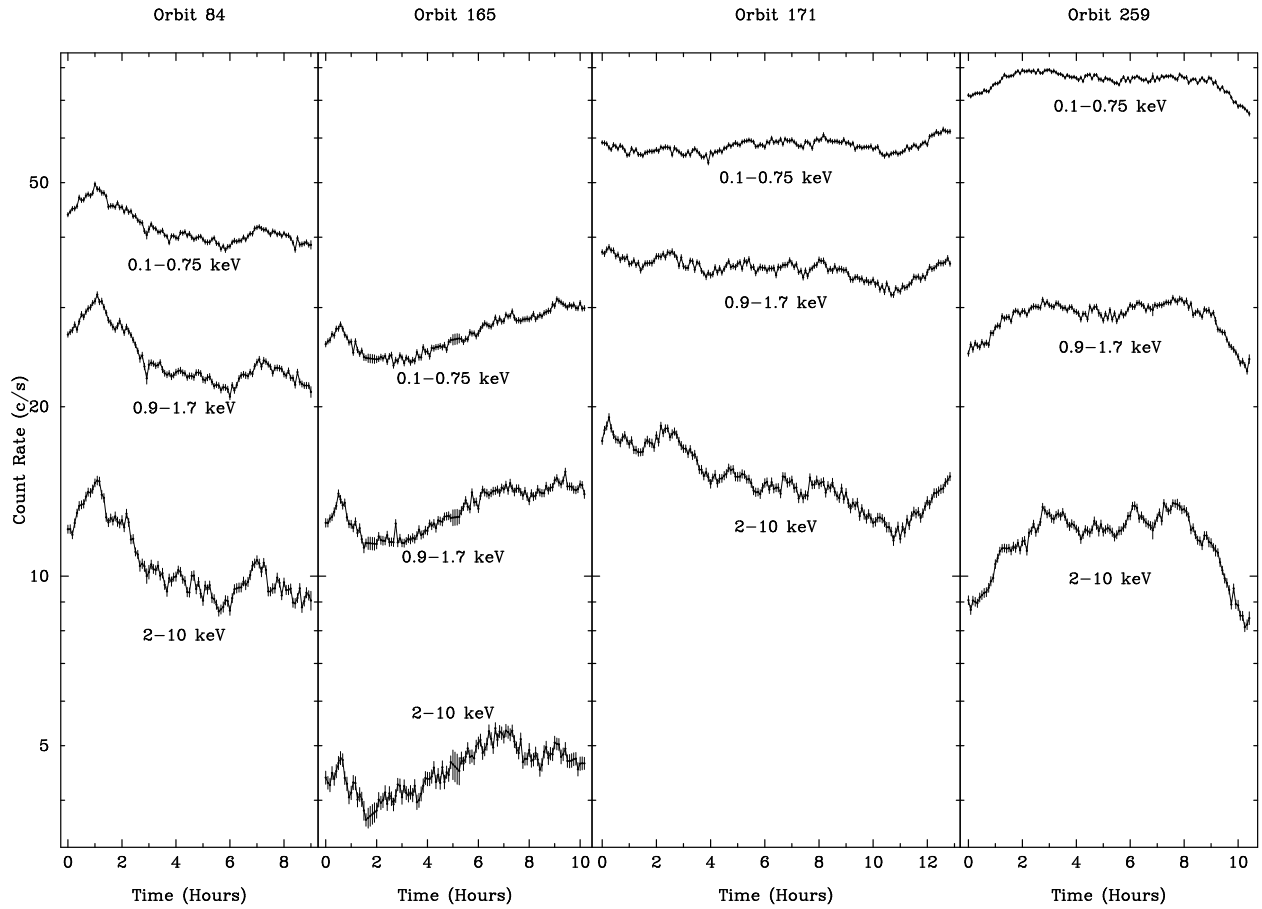


Fig. 1.— Grid of observed *XMM-Newton* pn light curves for Mkn 421. The Orbit 84 data are shown on the left (2000 May 25) through to Orbit 259 (2001 May 8) on the right.

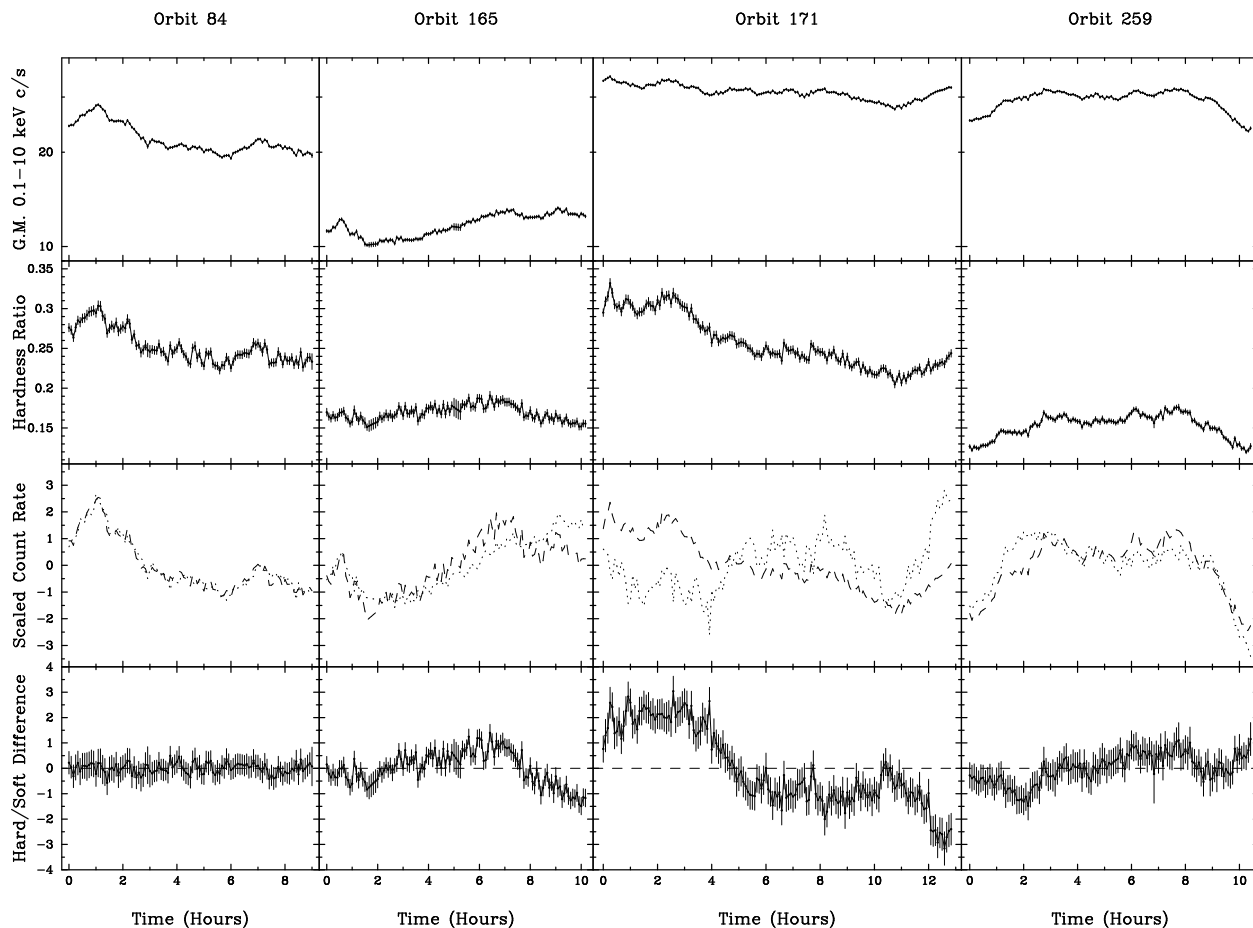


Fig. 2.— Grid of light curves of derived quantities. From the top, the light curves shown are the geometric mean count rate, 2–10 keV/0.1–0.75 keV hardness ratio, and overplot diagrams and difference diagrams (see text for details). In the overplot diagrams the soft band is denoted by the dotted line and the hard band is denoted by the dashed line. Note in particular that the hard and soft light curves track very well during O84 and O259, indicating a good correlation between bands, but not during O165 and O171, indicating that those data are less well-correlated.

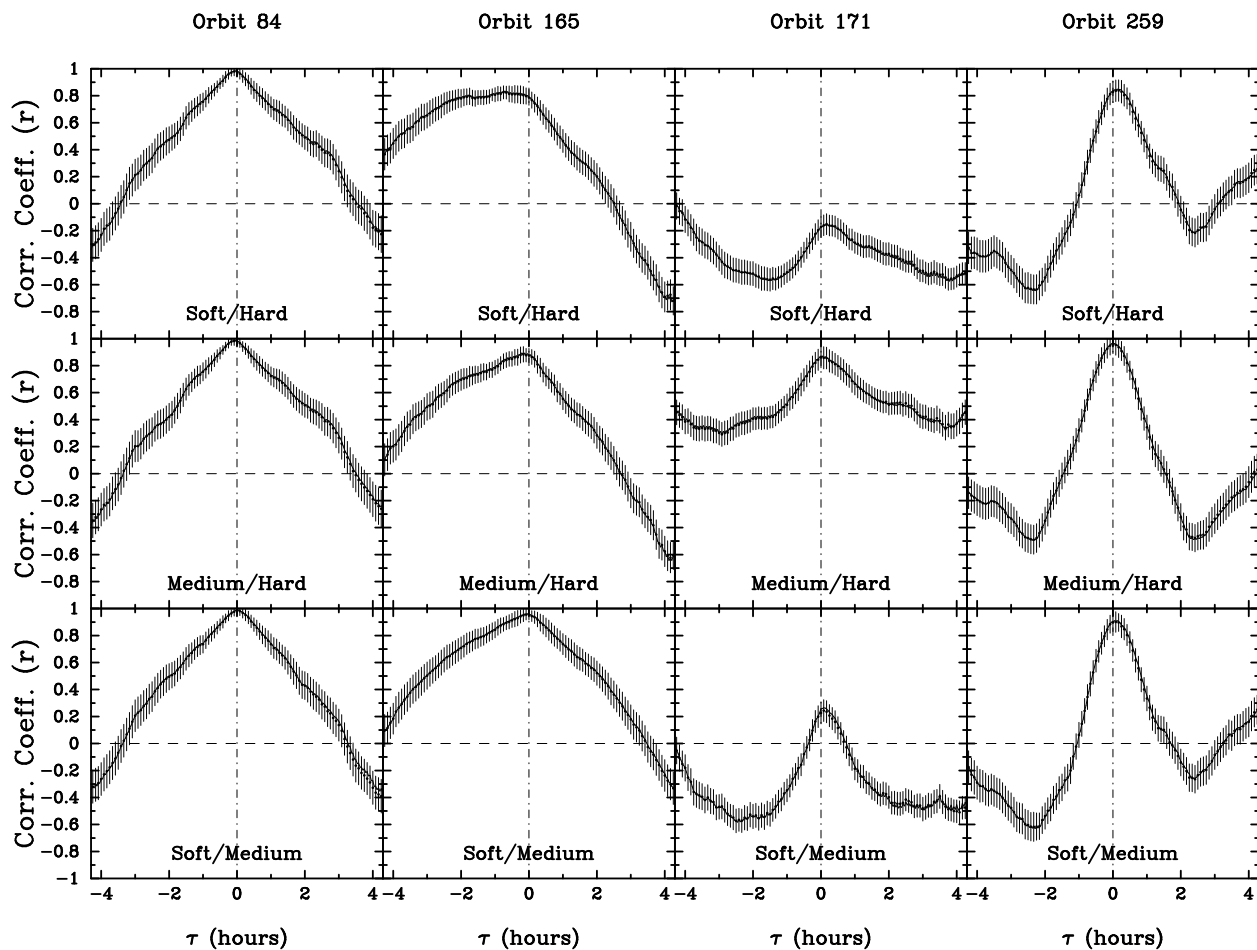


Fig. 3.— Grid of interband CCFs. The hard/soft band CCFs are shown on the top, hard/medium band CCFs in the middle, and medium/soft band CCFs on the bottom. Only the O84 and O259 data show a usable correlation, and those data are consistent with zero lag (to 2σ limits of $\lesssim 0.3$ ksec).

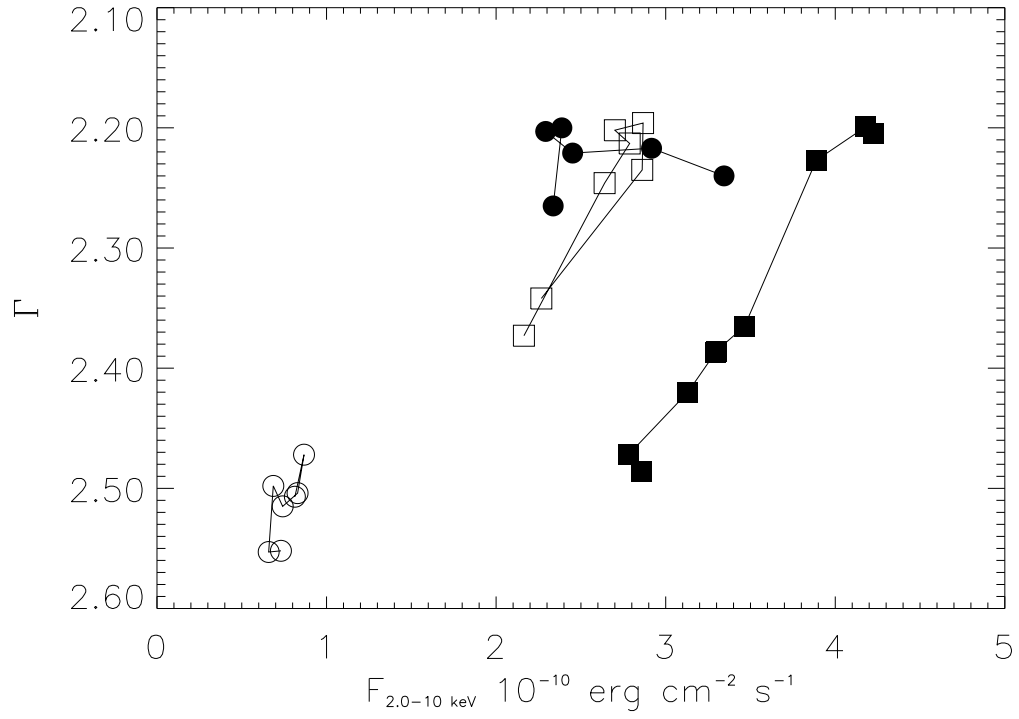


Fig. 4.— EPIC-pn photon spectral index in the 2.0-10 keV band plotted against the deabsorbed 2.0-10 keV flux. O84 are the closed circles. O165 are the open circles. O171 are the closed squares and O259 are the open squares.